Investigating Defect Detection in Advanced Ceramic Additive Manufacturing Using Active Thermography

Anthonin Demarbaix [1,*], Enrique Juste [2], Tim Verlaine [1], Ilario Strazzeri [1], Julien Quinten [1] and Arnaud Notebaert [1]

[1] Science and Technology Research Unit, Haute Ecole Provinciale de Hainaut Condorcet, Boulevard Solvay 31, 6000 Charleroi, Belgium; tim.verlaine@condorcet.be (T.V.); ilario.strazzeri@condorcet.be (I.S.); julien.quinten@condorcet.be (J.Q.); arnaud.notebaert@condorcet.be (A.N.)

[2] Belgian Ceramic Research Center (INISMa-CRIBC), Avenue Gouverneur Cornez, 4, 7000 Mons, Belgium; e.juste@bcrc.be

* Correspondence: anthonin.demarbaix@condorcet.be

Abstract: Additive manufacturing of advanced materials has become widespread, encompassing a range of materials including thermoplastics, metals, and ceramics. For the ceramics, the complete production process typically involves indirect additive manufacturing, where the green ceramic part undergoes debinding and sintering to achieve its final mechanical and thermal properties. To avoid unnecessary energy-intensive steps, it is crucial to assess the internal integrity of the ceramic in its green stage. This study aims to investigate the use of active thermography for defect detection. The approach is to examine detectability using two benchmarks: the first focuses on the detectability threshold, and the second on typical defects encountered in 3D printing. For the first benchmark, reflection and transmission modes are tested with and without a camera angle to minimize reflection. The second benchmark will then be assessed using the most effective configurations identified. All defects larger than 1.2 mm were detectable across the benchmarks. The method can successfully detect defects, with transmission mode being more suitable since it does not require a camera angle adjustment to avoid reflections. However, the method struggles to detect typical 3D-printing defects because the minimum defect size is 0.6 mm, which is the size of the nozzle.

Keywords: active thermography; additive manufacturing; ceramic

1. Introduction

Pottery objects crafted using the potter's wheel are categorized under traditional ceramics, alongside porcelain items. These objects, made from clay, are shaped and fired to form a hard, durable surface. According to the American Society for Testing and Materials (ASTM) C28, "Advanced Ceramic" refers to a "highly engineered, high-performance, predominantly nonmetallic, inorganic material with specific functional attributes" [1]. Advanced ceramics are generally divided into two categories: engineering ceramics and functional ceramics.

Functional ceramics are primarily used in the electronics industry due to their unique physical properties. On the other hand, engineering ceramics—also known as technical ceramics—are further classified into oxides, carbides, nitrides, borides, silicates, and glass ceramics [2,3]. Table 1 highlights some of the most commonly used engineering ceramics in industry, along with their key properties, including low density, high hardness, and high flexural strength.

Engineering ceramics offer several significant advantages, including exceptional durability, hardness, biocompatibility, and mechanical strength at elevated temperatures. They also exhibit excellent chemical inertness when compared to metals and engineering polymers. Unlike metals and polymers, which can degrade in corrosive, abrasive environments

and at high temperatures, engineering ceramics maintain their performance in such conditions. These properties make them highly competitive in a variety of engineering fields, including aerospace, automotive, biomedical, electrical, and chemical engineering [2].

Table 1. Material properties of commonly employed technical ceramics for structural applications: indicative value across different commercially available grades [2].

Material Properties	Al_2O_3	Si_3N_4	ZrO_2	SiC
Density (g/cm^3)	3.8–4.0	3.2	5.0–6.0	3.1
Vickers hardness (kg/mm^2)	1800–2000	1500–1600	1100–1300	2600
Fracture toughness (MPa $m^{1/2}$)	3–4	4–8	4–12	3–5
Flexural strength (MPa)	300–500	700–850	500–1800	400–600
Young's modulus (GPa)	300–400	310	200	400–450
Thermal conductivity (W/mK)	25–35	30–40	1.5–2	80–120

Ferraris et al. [2] proposed various manufacturing processes used to shape complex ceramic components. Figure 1 illustrates these different manufacturing chains.
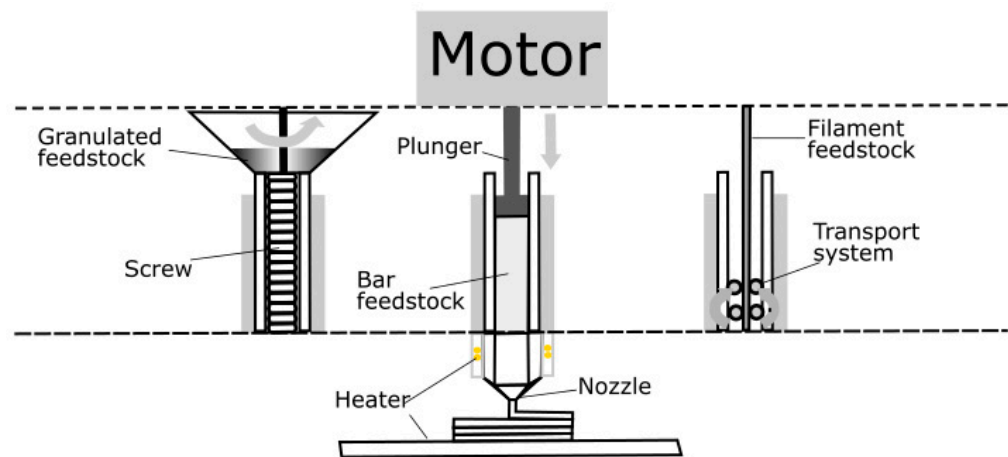

Figure 1. The three different mechanisms for MEX additive manufacturing.

The traditional ceramic manufacturing process begins with powder preparation and ends with final machining, with powder characteristics like composition and size being crucial for product quality. In modern practices, green bodies are machined to reduce crack formation, though parameters are often empirically set, limiting repeatability. After machining, additives like binders and plasticizers are removed through heat treatment to avoid negatively affecting the sintering process [2].

Machining dense ceramics is possible but requires costly diamond-coated tools due to the material's brittleness and high strength, leading to potential fractures, rapid tool wear, and slow processing [4]. Grinding is another conventional method for modifying ceramic surfaces, and nontraditional techniques are also used [5,6].

Additive manufacturing offers new approaches for complex ceramic shapes, with both direct and indirect methods. In some cases, debinding and sintering are required, taking shrinkage into account.

Additive manufacturing (AM) technologies were initially developed for rapid prototyping, allowing designers to visualize product concepts. However, these technologies have since evolved into a booming field for producing small series of functional parts with impressive mechanical properties. AM is particularly prominent in the biomedical and aerospace industries, as well as in rapid tooling applications. The key advantage of AM is its ability to produce highly complex designs that are difficult or impossible to achieve with traditional manufacturing methods. This is accomplished by building the product layer by layer, adding material incrementally [7].

Various AM technologies used for shaping ceramics are categorized into three groups based on feedstock form: slurry-based, powder-based, and solid-based.

Selective laser melting is one of the direct methods for shaping ceramics, but it requires the use of two laser sources to preheat the powder bed before shaping or advanced thermal management to prevent cracks occurrences [2,8–10]. Currently, direct ink writing and laminated object manufacturing are the most cost-effective AM technologies, although they tend to produce surfaces with lower quality. On the other hand, technologies that offer superior surface quality tend to be more expensive.

Slurry-based 3D-printing technologies use liquid or semiliquid systems in which ceramic particles are dispersed as feedstock. In contrast, powder-based 3D-printing technologies rely on powder beds of loose ceramic particles, which are bonded either by spreading liquid or by powder fusion using thermal energy. Lastly, solid-based 3D-printing technologies use solid ceramic feedstock, such as sheets or 3D filaments doped with ceramic particles [2,8,9].

Material extrusion (MEX) additive manufacturing is designed to produce components with a high build rate and lower cost per part compared to other additive manufacturing techniques. One of its key advantages is its versatility, enabling the additive manufacturing of a wide range of materials, including metals, composites, and ceramics. While no industrial or mainstream ceramic products are currently manufactured using MEX, research on shape stability during printing and sintering is rapidly advancing, indicating that this process will soon find practical applications in various industries.

The MEX process involves four main stages: feedstock preparation, 3D printing, debinding, and sintering. The feedstock consists of a homogeneous mixture of metal or ceramic powders combined with binders. During the 3D-printing stage, material extrusion is synchronized with the movement of the table or extrusion head. There are three possible feeding systems: a pinch feed mechanism using spooled filament, and syringe/piston-based or screw-based extrusion systems, which use pelletized feedstock from the powder injection molding (PIM) industry [11,12].

Figure 1 shows the three existing variants for MEX.

Rane et al. [11] discussed the influence of various printing parameters on the mechanical characteristics of ceramics produced through extrusion-based additive manufacturing. It focuses on the relationship between printing parameters, such as layer height, print speed, and extrusion rate, and how they affect the density, porosity, and mechanical strength of the final ceramic parts. Their study highlighted the importance of optimizing these parameters to improve product quality, specifically enhancing properties such as strength, structural integrity, and surface finish. The weight changes were observed in parts during various stages of the extrusion-based additive manufacturing process: from the initial green state through solvent debinding, thermal debinding, and sintering. After solvent debinding, a portion of the weight was lost due to the removal of water-soluble binder components. During thermal debinding, an additional weight loss occurred as the backbone binder was eliminated. In the sintering phase, there was an unexpected further reduction in weight, primarily due to the removal of residual binders and some loss of powder. The total weight loss expected after sintering, based on the feedstock composition, was consistent for alumina and zirconia parts, with the data showing similar weight reduction across all parts, regardless of the extrusion velocity used.

The indirect additive method produces a semifinished green ceramic part as an intermediate stage in the process. However, the internal integrity of the part is typically not evaluated until after the sintering cycle, despite the potential for defects arising during the 3D-printing phase. Additionally, in its green state, the ceramic part can be more easily recycled, offering significant environmental benefits by avoiding the need for a sintering cycle. This enhances the sustainability of the process by facilitating easier material recovery and reuse.

Zhao et al. [13] provided a comprehensive overview of the various nondestructive testing (NDT) methods used to detect defects in ceramic materials. Ceramic defects can

significantly impact the material's performance, particularly in high-stress applications. These defects include cracks, pores, voids, inclusions, surface imperfections, delamination, and distortion. Cracks, often caused by thermal or mechanical stresses during cooling and sintering, can be detected using ultrasonic testing, which analyzes wave reflection at defect interfaces, or acoustic emission, which monitors real-time crack formation and growth during stress.

Pores and voids, which are typically formed due to improper densification, can be identified through X-ray tomography, which generates detailed 3D images of the ceramic's internal structure. Ultrasonic testing can also detect voids, although it may be less effective for large volume defects. Inclusions, or foreign particles embedded within the ceramic matrix, can weaken the material. X-ray tomography and laser ultrasonic techniques are ideal for detecting these inclusions by providing high-resolution internal imaging.

Delamination, the separation of layers in laminated ceramics, is often the result of poor bonding. Ultrasonic testing can detect delamination by analyzing wave propagation through layers, and acoustic emission can monitor for delamination during stress application.

Distortion, or warping, caused by uneven heating or cooling during sintering, can lead to misshapen parts. Machine vision is effective for detecting external distortion, while X-ray tomography can assess internal shape distortions. Each NDT method offers unique strengths depending on the type of defect, with ultrasonic testing being versatile for both surface and internal defects, and X-ray tomography excelling at identifying internal flaws like pores and inclusions. Machine vision is ideal for surface defect detection, while infrared thermography provides a noncontact method to detect surface temperature variations. Acoustic emission is particularly useful for real-time monitoring of defect growth under stress.

Infrared thermography (IRT) is used for detecting surface defects in ceramics by measuring temperature differences. This method captures infrared radiation emitted from the ceramic surface, allowing for the identification of surface anomalies such as cracks, delamination, or voids caused by defects. While thermography is particularly useful for surface inspections, its ability to detect internal defects is limited. The technique's sensitivity and accuracy depend on the spatial resolution of the infrared camera, making it best suited for applications where surface integrity is critical. In addition, the reflective aspect of the material can lead to detection problems. Garrido et al. [14] suggest tilting the sample to minimize the reflective aspect of the sample.

For additive manufacturing, X-ray microcomputed tomography (μCT) is the most commonly employed NDT technique for evaluating the internal structure of ceramic implants produced. μCT offers high-resolution, three-dimensional imaging of both the internal and external features of implants, making it particularly well suited for detecting critical structural irregularities such as pores, cracks, and delamination. These defects, if left undetected, can compromise the mechanical integrity and overall performance of the implant, highlighting the importance of μCT in ensuring quality control and reliability in medical applications [15].

In additive manufacturing, thermographic testing is used to monitor the heat diffusion in materials, which helps in detecting anomalies like cracks, porosity, and delamination. Various thermal excitations, such as hot air or ultrasounds, are applied to enhance the thermal contrast and improve defect detection reliability. Despite its limitations, thermography remains a valuable tool for surface-level monitoring in additive manufacturing, especially when used alongside other NDT techniques [15]. For example, Makipour et al. [16] used an infrared camera; the authors analyzed the thermal evolution of ABS filament layers, investigating temperature distribution and heat accumulation during fabrication. Insights from these thermal data help optimize process parameters, improving surface quality, mechanical properties, and reducing common defects in additive manufacturing.

Active thermography is increasingly being applied to composite material inspections, capitalizing on the heat transfer characteristics of materials to detect subsurface defects by measuring surface temperature or the rate of temperature change at the surface. This

technique is typically used for area-based inspections and is characterized by its relatively high speed. Active thermography can be implemented in two modes: transmission, where the component is positioned between the heat source and the infrared camera, or reflection, where both the heat source and the camera are on the same side of the object. This method requires thermal excitation of the inspected area, followed by the measurement of surface irradiance or temperature. Figure 2 shows the physical principle of the method.
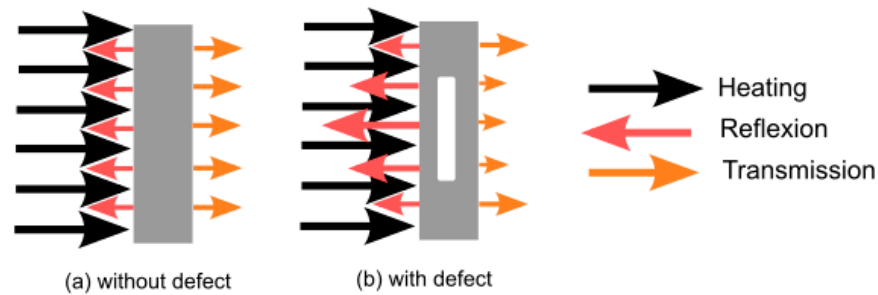
Figure 2. Physical principal of active thermography.

The fundamental principle of active thermography can be summarized as follows:

- The surface is irradiated by an external heat source.
- The material emits infrared radiation, the intensity of which is influenced by factors such as the duration of exposure to the heat source (a).
- If the heat flux encounters a defect (b), the infrared emission pattern is altered, which enables defect detection.

Both reflection and transmission modes are viable for this inspection technique, but transmission has shown superior results in detecting porosity in composites. This is primarily due to the influence of heat flux during the cooling phase and the condition of the exposed surface [17].

For thermography-based inspections, an infrared camera is required to capture surface temperature over time within its field of view. It is important to note that this method has limitations in terms of defect depth detection due to thermal flux constraints. A general rule of thumb is that the detectable defect must have a lateral dimension greater than its depth within the component [18].

Thermographic inspections can be performed in either a "passive" or "active" mode. In passive thermography, the natural environment provides the thermal excitation without the need for external heat sources. In contrast, active thermography involves external thermal stimulation. The heat transfer between the surface and the heat source in active thermography is described by the following equation:

$$T_s(t) - T_s(0) = \frac{Q}{K\rho C(\pi t)^{\frac{1}{2}}}, \tag{1}$$

where

- T_s is the surface temperature;
- Q represents the input energy delivered by the external heat source;
- t is the time elapsed since the thermal pulse;
- K is the material's thermal conductivity, ρ is the material's density and C is its specific heat capacity.

This equation demonstrates that, under normal conditions, the temperature evolution over time forms a straight line with a slope of 0.5 on a logarithmic plot. However, when a discontinuity or internal defect is present, this slope changes. By employing thermographic signal reconstruction (TSR) techniques on the infrared image sequences, it is possible to significantly enhance the sensitivity of defect detection [18].

Nevertheless, the infrared camera data can be subject to various disturbances such as external reflections, variations in optical properties, and uneven heating, all of which introduce abnormal thermal profiles in the thermograms, complicating the detection and characterization of defects. These issues are addressed by using advanced signal processing techniques that not only reduce noise but also improve thermal contrast, thereby enhancing defect detection and quantification capabilities [19].

In laminated composites, the observed thermal contrast decreases as the orientation angle between adjacent layers increases, making defect detection in cross-ply or multiangle laminates more challenging compared to unidirectional laminates. This difficulty is particularly pronounced in carbon-fiber-reinforced polymer (CFRP) laminates, where the high thermal conductivity of carbon fibers limits the depth detection capability of the thermography method [20,21]. Due to these constraints, despite its inherent advantages, thermography is generally not the primary inspection method used in the aerospace industry.

The goal of this paper is to introduce an active infrared thermography technique as a nondestructive method for inspecting ceramics in their green stage, aiming to improve internal defect detection before the sintering cycle. Since the binder is a thermoplastic, the active thermography method can be applied using an appropriate heat source that allows for heat transmission within the material, as the final thermal properties of the ceramic have not yet been achieved. This method offers a cost-effective solution for early detection of internal flaws. This paper explores the feasibility of applying this approach by first outlining a general methodology, and then focusing on its specific application in ceramic additive manufacturing processes.

2. Materials and Methods

2.1. Benchmark Printing

The first step is to print the benchmarks that will serve as a working basis for studying the feasibility of nondestructive infrared testing.

2.1.1. 3D Printer

The printer used in this study is a Pellet Additive Manufacturing (PAM) system from Pollen AM (Ivry-sur-Seine, France), specifically the PAM MC Series C, which operates on the principle of material extrusion via an endless screw printhead. This open-parameters 3D printer is designed for processing high-performance materials, including polymers, metals, and ceramics, using feedstocks primarily designed in the powder injection molding (PIM) process.

Temperatures and manufacturing conditions based on the INMAFEED K1008 datasheet were used to print benchmark designs.

2.1.2. Composite Feedstock

The selected feedstock for the PAM process was INMAFEED K1008 from INMATEC Technologies GmbH (Rheinbach, Germany). The feedstock is based on an alumina powder (Al_2O_3, 96%, KMS-96 BO (Martinswerk, Bergheim, Germany)) and a thermoplastic binder, which is a polyolefin-based binder system. The shrinkage factor stated by the pellet manufacturer is 1.18.

2.1.3. Benchmark Design

The benchmarks are produced by automatically introducing defects into the CAD model to generate intentional air pockets. This approach requires printing without support structures, allowing the printer to form the air pockets as designed. Figure 3 shows the external appearance of the benchmarks post-printing, demonstrating successful defect formation and the overall print quality. Indeed, no collapse of the upper wall is observed on the benchmark.

Two different porosity designs were chosen. The first is a classic benchmark in the shape of either a square or a disc whose size decreases in order to detect a threshold for

the use of the method. Defects are generated directly by the 3D printer because they have been modeled in the benchmark design. The height of the defects was determined using exploratory testing to ensure that there was no dropout during printing. Figure 4 shows a schematic view of benchmark B1, called benchmark "detection threshold", which will be used as a reference benchmark for defect detection. The depth of the defects is variable at 0.9 mm, 1.2 mm, and 1.5 mm.
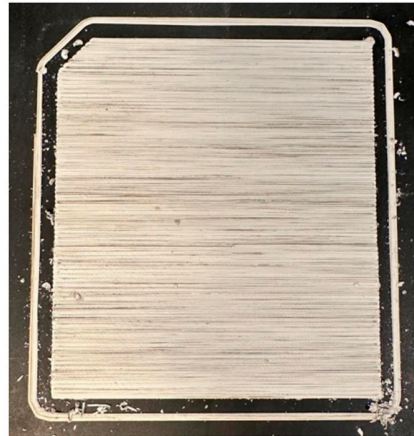

Figure 3. External appearance of benchmarks at the end of 3D printing.
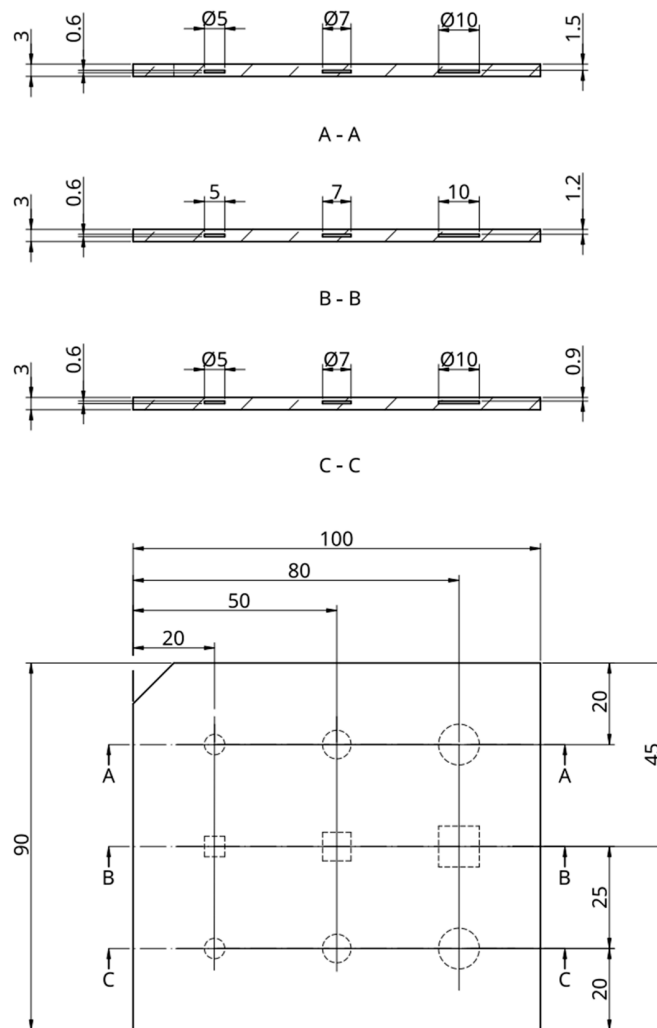
Figure 4. Schematic view of benchmark B1 called benchmark "detection threshold".

Benchmark B2, called benchmark "defect printing", relates to the manufacturing process, and a schematic view is shown in Figure 5. The defect simulated is a printhead clogging for a short period, resulting in a lack of filament on one of the layers. Modeling is carried out using an empty rectangle in the print. The depth, length, and width vary in order to take into account the variability of the process on layer deposition, which depends on the various printing parameters.
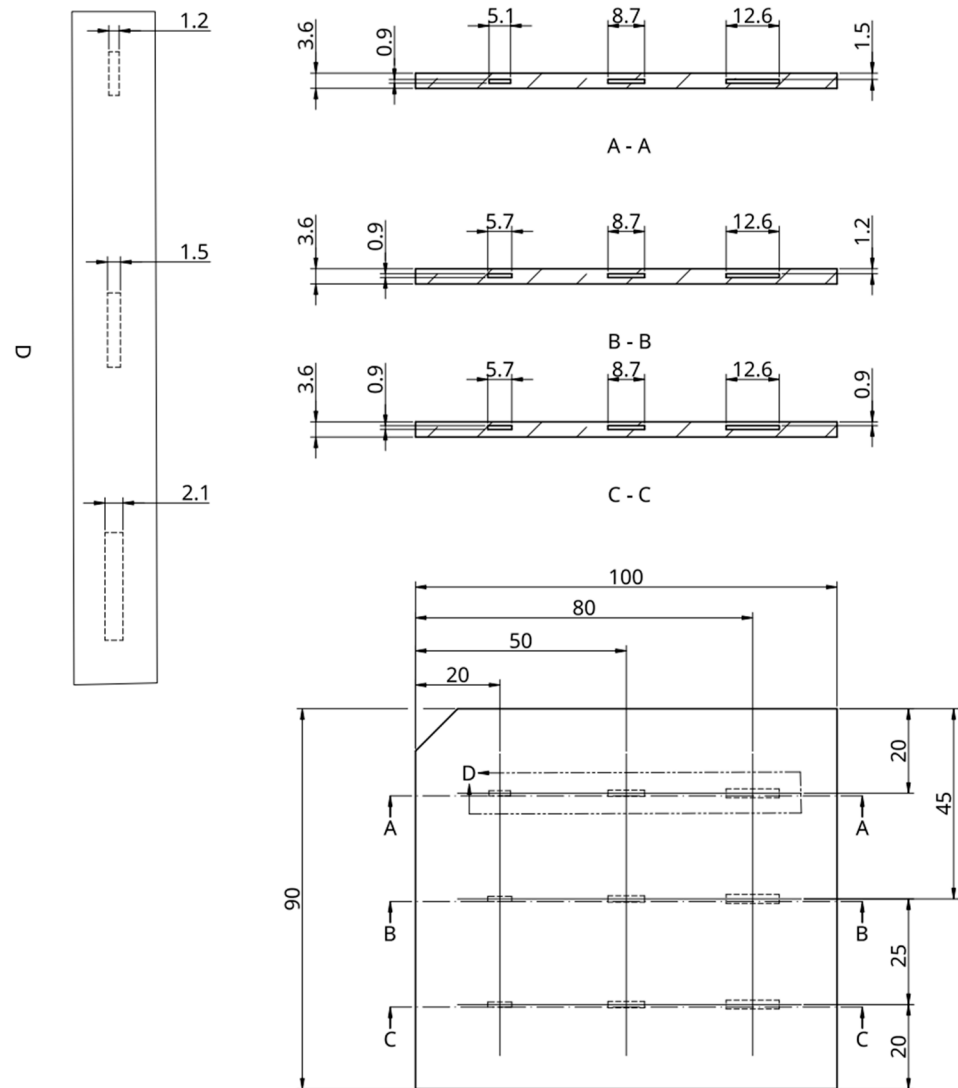
Figure 5. Schematic view of benchmark B2 called benchmark "defect printing".

2.2. Experimental Setup

For this study, the experimental setup was used to carry out active thermography. The setup consisted of two 1000 W halogen lamps, each mounted on a tripod, and the thermal response of the sample was recorded with an FLIR T865 infrared camera located at the same distance, featuring a 10 mm (42°) lens and NETD thermal resolution < 0.03 °C (<30 mK). The thermal camera operates in a spectral band ranging from 7.5 μm to 14 μm. The invariable characteristics of the experiments carried out in this research, i.e., the lamp/benchmark distance, the pulse time, and the beta angle of the lamps (see Figure 6), were derived from the use of a numerical model developed by Notebaert et al. [22] to determine an operating point. The lamps were positioned 40 cm from the benchmark, and the benchmark was heated during a 20 s pulse, with a total observation time of 60 s. The software used to analyze the thermal response was FLIR Tools 6.4.
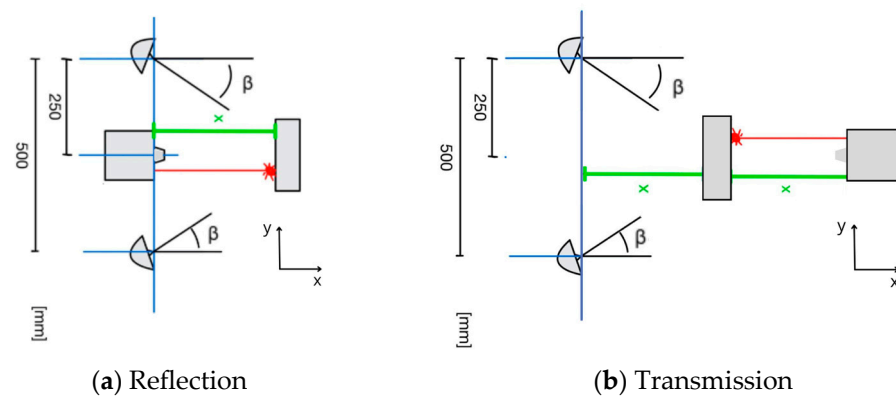
(**a**) Reflection (**b**) Transmission

Figure 6. Schematic view of the experimental setup: (**a**) reflection mode and (**b**) transmission mode.

Two types of inspection were carried out on the benchmarks: reflection and transmission thermography. By reflection, this means that the camera is located on the same side as the excitation source, which is the case observed in Figure 6a. In the case of transmission, we position the camera on the other side of the sample to be observed, as can be seen in Figure 6b. In this study, during the transmission tests, the different parameters used in the case of reflection were maintained by placing the sample equidistant from the lamps and the camera.

In addition to the lamp/benchmark distance, other parameters were set during the tests, such as the β angle shown in Figure 6, which is the angle given to the lamps and is 20°. The infrared camera was also tilted to avoid reflections and, thus, improve the results obtained from the reflection emanating from the benchmark's surface due to its material properties. This tilt, denoted α in Figure 7, has a value of 25°.
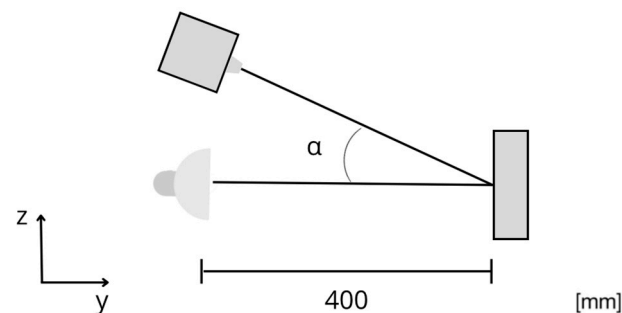
Figure 7. Schematic view of the camera tilt in the experimental setup.

Post-processing is required to highlight any flaws in the part. Ebrahimi et al. [23] proposed to use a temporal post-processing called PCT to obtain a fast processing time and a detection between healthy and defective areas. Principal component thermography (PCT) is a technique used for detecting defects in materials like composites by analyzing thermal data. It is based on principal component analysis (PCA), a statistical method that compresses high-dimensional data into a lower-dimensional space, highlighting differences in the data. This helps to enhance the contrast between defective and nondefective areas, making flaws easier to detect. PCT is effective for defect contrast enhancement and data compression, but it is sensitive to noise, which can affect the accuracy of defect detection in noisy environments. This post-processing was carried out using IR View software, followed by image processing using Maestro to measure the defects.

3. Results

The results are presented in two distinct parts. The first focuses on determining the optimal positioning of both the camera and the heating system. This step makes it possible to choose the most suitable configuration for reflection and transmission analysis. The

second part evaluates the most effective sequence for assessing the feasibility of detecting common defects in 3D printing.

In each section, raw images captured during the heating and cooling phases are available, illustrating the evolution of temperature throughout the test. While external environmental factors introduce noise to the raw data, this does not hinder the detection of defects, as the detection process relies primarily on contrast curves and relative temperature differences. To interpret results, PCT removes the noise generated by external conditions.

3.1. Benchmark B1

Table 2 presents the temperature evolution during both the heating and cooling phases for each configuration. In all the raw images, defects become visible during the heating phase of the sample, but not during cooling. At a reflection angle of 0°, defect detection proves to be challenging. Additionally, thermal nonuniformity is observed during cooling, with a localized area exhibiting higher temperatures.

Table 2. Raw results of thermography on benchmark B1.

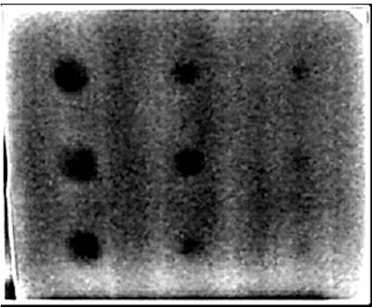| Mode	Heating		Cooling			
	t = 10 s	t = 20 s	t = 30 s	t = 40 s	t = 50 s	t = 60 s
Reflection 0°						
Reflection 25°						
Transmission 0°						
Transmission 25°						
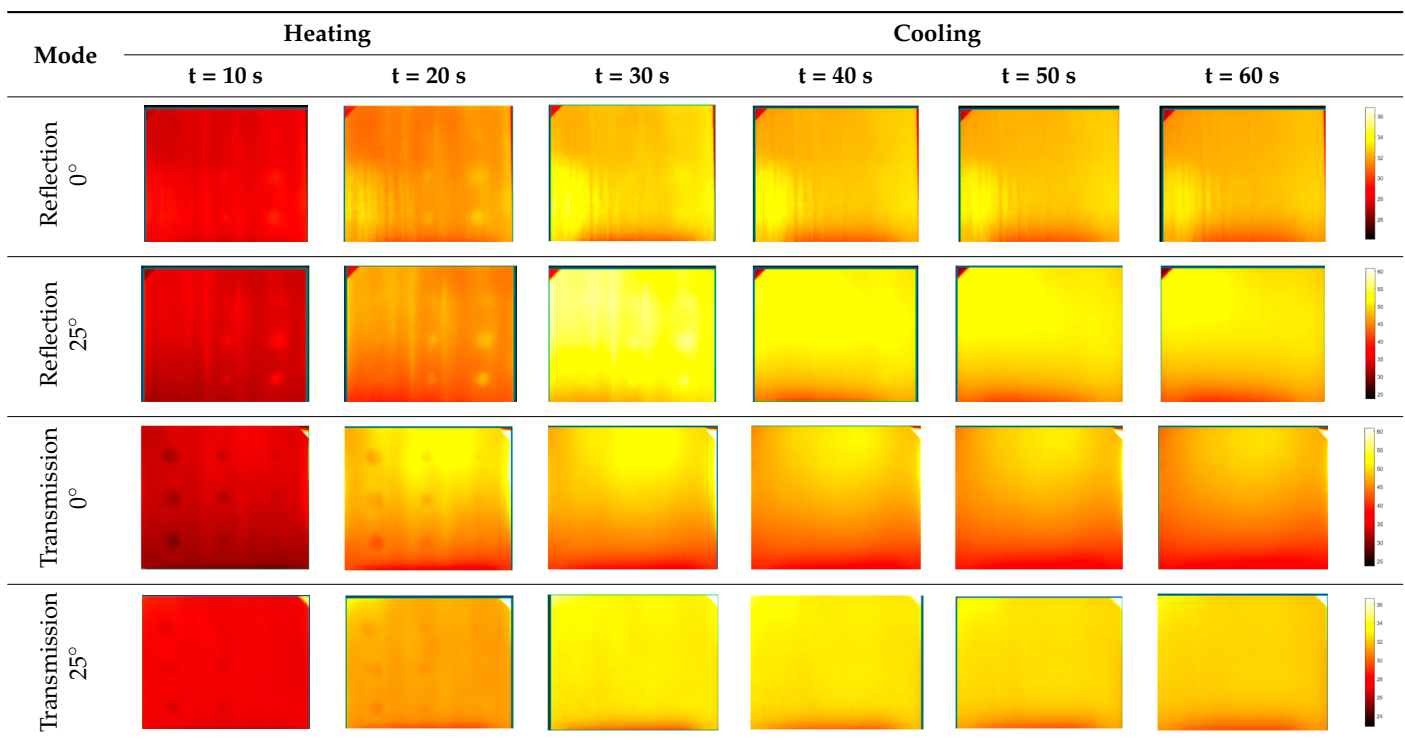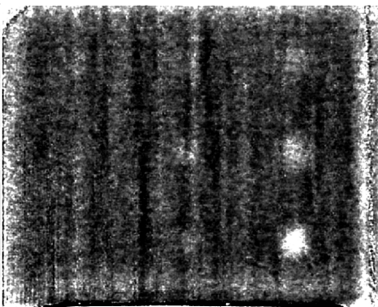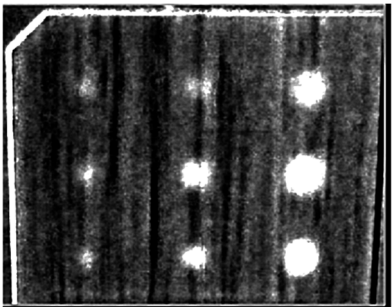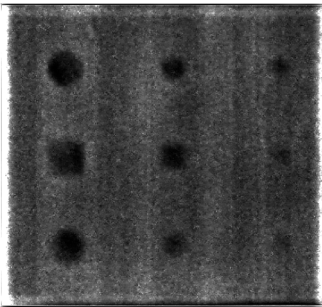
Table 3 illustrates the PCT results for reflection and transmission at both angles for benchmark B1. The initial observation is that all defects are detected, except for reflections at a 0° angle, where smaller defects are harder to identify. In fact, only the three biggest defects are visible but not clearly identified. At a 25° angle, reflection interpretation becomes challenging, primarily due to the shape of the defect. In this configuration, distinguishing between square and circular defects is not feasible.

In transmission mode, all defects are detected, regardless of size. However, shape detection becomes difficult to interpret at a 25° angle. Conversely, PCT transmission at a 0° angle successfully detects all defects and their shapes. Among all configurations, this is the only one that reliably distinguishes both the type and size of defects.

Table 3. PCT results of thermography on benchmark B1.

	Angle of 0°	Angle of 25°
Reflection		
Transmission		

3.2. Benchmark B2

Table 4 depicts the thermogram evolution during the heating and cooling phases. A notable observation is the crucial impact of surface condition on reflectivity. Irregularities resulting from bead junctions on the surface introduce inconsistencies in the thermographic data. This underscores the challenge of interpreting the results accurately without post-processing. In fact, the raw images alone make it difficult to clearly discern defects in the configurations presented.

Table 4. Raw results of thermography on benchmark B2.
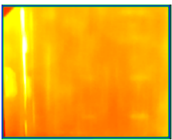
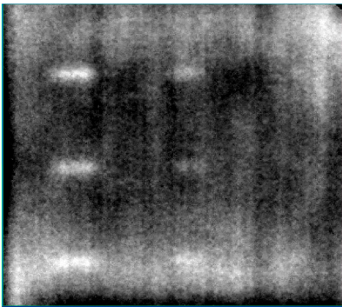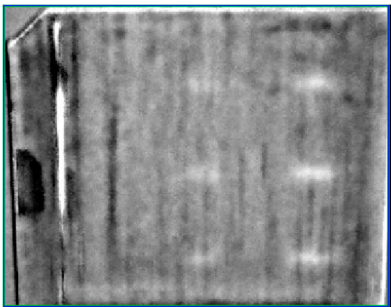| Mode	Heating			Cooling		
	t = 10 s	t = 20 s	t = 30 s	t = 40 s	t = 50 s	t = 60 s
Reflection 25°						
Transmission 0°						

Table 5 shows the PCT results for the favorable reflection case and the favorable transmission case.

In reflection mode, a mark is visible on the left side, representing a surface irregularity on the benchmark, which does not affect the detection of other defects. Similar to benchmark B1, the number of detectable defects is the same for both 25° reflection and 0° transmission. The observation holds true for shape detection as well, where interpreting a rectangle is easier in transmission than in reflection. Lastly, defects with a width of 1.2 mm remain undetectable.

Table 5. PCT results of thermography on benchmark B2.

Transmission 0°	Reflexion 25°

4. Discussion

Figure 8 illustrates the PCT of benchmark B1 following image processing using Maestro software, which enhances contrast to highlight defects.
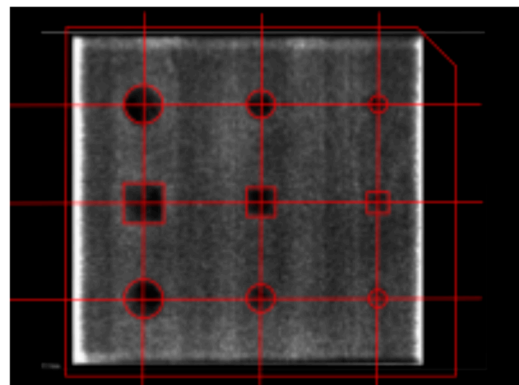
Figure 8. PCT of benchmark B1 in 0° angle transmission with shape tracing.

A plot of the shapes was added to show that they are clearly distinguishable, regardless of their size. This clarity is achievable thanks to the 0° transmission mode, where the camera is positioned in normal direction to the plate, capturing only the heat transmitted through the material from the source. In reflection mode, the source's reflection is directly focused on the camera, making defects difficult to identify. This issue is further exacerbated by the polished surface of the sample, which is in contact with the printing plate, causing the thermal camera's sensors to become saturated. This results in poor image quality and unreliable interpretation. With a 25° angle, the reflection from the source no longer aligns directly with the camera, improving defect detection, though not significantly. The angle of the camera introduces vertical distortion, transforming square defects into oval shapes, which complicates result interpretation. This distortion is also present in transmission mode, but it is less severe due to the absence of noise from reflected light.

In the case of benchmark B2, no configuration is capable of detecting defects as small as 1.2 mm in width, revealing the limitations of the detection method for additive green ceramics. This underscores the technique's inability to identify "blocked nozzle" defects over a given period. In this context, the bead width corresponds to the nozzle diameter, which is 0.6 mm. Such defects remain undetected because the method requires a minimum of three passes to reveal them, with the smallest detectable size being 1.5 mm. However, if the defect is near or on the surface, it becomes immediately visible to the camera. This is illustrated in transmission mode, where a surface defect, such as a missing pass of material, is easily detected. Even though the defect is captured in transmission mode, it generates significant noise, complicating the internal analysis of the part.

Upon further analysis, the observation is similar to that of benchmark B1, where vertical distortion results in the rectangle appearing oval. However, the length-to-width ratio allows for the defect's length to be clearly identified, enabling accurate interpretation along this axis. Despite the camera being tilted at 25°, the length of the defect is still accurately conveyed. The tilt only introduces distortion along the vertical axis, leaving the horizontal axis unaffected.

Figure 9 presents the most relevant results from each reference test, focusing on defect quantification. The method used to quantify defects involves analyzing the histogram of gray levels along the profile to accurately identify the area corresponding to the defect, resulting in more precise measurements. The histogram visually represents the pixel intensity distribution across different gray levels, showing the number or proportion of pixels at each level and offering a concise overview of the image's tonal range.
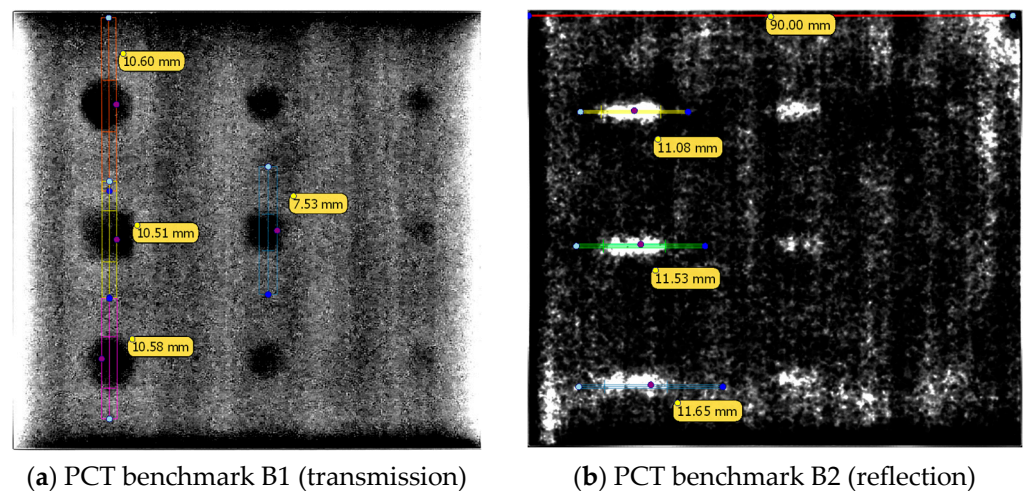

(**a**) PCT benchmark B1 (transmission)   (**b**) PCT benchmark B2 (reflection)

Figure 9. Measurement of the largest defects on PCT: (**a**) benchmark B1 and (**b**) benchmark B2.

For benchmark B1, transmission at a 0° angle was chosen, enabling clear distinction of each shape. Measurements were taken for each large defect in the first column, corresponding to a side (or diameter) of 10 mm. Measurements taken on the benchmark reveal a deviation of up to 0.6 mm, despite the favorable configuration for detection. Even the square, which should have a side length of 7 mm, exhibits this deviation. These results indicate that the heating parameters require optimization to enhance the accuracy of the method.

In the case of benchmark B2, reflection at an angle of 25° was used to quantify the length of the defect, whose nominal measurement is 12.6 mm. The deviation observed in this case is approximately 1 mm. This is a direct impact of benchmark B1, where the configuration is less favorable than in the previous case due to the material's reflective properties.

In perspective, optimizing the heating parameters will enhance the accuracy of the method in transmission mode, which will, in turn, positively affect the performance in reflection mode at an angle. In the case of reflection, fine-tuning the angle of inclination could further improve quantification in this configuration

5. Conclusions

Additive manufacturing with advanced materials, such as technical ceramics, is gaining prominence. Ceramic additive manufacturing can be performed either directly or indirectly. In the indirect process, the manufacturing chain includes debinding followed by sintering to achieve the part's final properties. This final stage is relatively energy-intensive for producing ceramic components. While defects present in the earlier stages may be reduced due to material shrinkage, they remain and continue to weaken the part, ultimately reducing its mechanical performance.

Detecting defects at the end of the additive manufacturing process, in the green ceramic state, is crucial for performing an intermediate assessment of the part's internal integrity before the final stage. Since the binder is a thermoplastic, the active thermography method can be applied with an appropriate heat source. At this stage, the ceramic particles are held in place by the binder, and the final thermal properties that allow the ceramic to function as a thermal barrier have not yet been fully obtained.

The method was tested on two separate benchmarks to assess its applicability to green ceramics and its ability to detect defects as small as 5 mm. This also allowed for an exploration of both reflection and transmission modes, as well as the importance of camera angle to avoid reflections from the material's polished surface in contact with the 3D printer platen. Table 6 summarizes the minimum size that can be detected with the method.

Table 6. Summary of minimum detectable size.

	0° Angle	25° Angle
B1—Reflection	>10 mm	>5 mm
B1—Transmission	>5 mm	>5 mm
B2—Reflection	/	>1.5 mm
B2—Transmission	>1.5 mm	/

The results showed that, in reflection mode, an angled configuration is necessary to detect defects larger than 5 mm. However, transmission mode with a 0° angle proves to be the optimal setup, as it allows for both detection and direct characterization of defects, with the camera positioned normal in the surface under analysis.

For common 3D-printing defects, the method unfortunately faces limitations due to its detectability threshold. For example, it struggles to detect blocked nozzle defects, where material is temporarily absent during printing. The smallest defect detected was 1.5 mm, while the target defect size, corresponding to the printing nozzle, is only 0.6 mm. Additionally, surface defects can interfere with the method's ability to accurately interpret the internal integrity of the part.

Finally, the defect size quantification reveals a deviation of 0.6 mm in the most favorable case, suggesting room for further optimization of the method. This optimization should also consider the camera's angle of inclination, as additional deviation is observed when an angle is introduced.

Author Contributions: Conceptualization, A.D., E.J. and A.N.; methodology, A.N. and T.V.; software, I.S. and A.N.; validation, A.D. and E.J.; formal analysis, A.D.; investigation, T.V. and A.N.; resources, A.D. and E.J.; writing—original draft preparation, A.D.; writing—review and editing, I.S., J.Q. and E.J.; visualization, A.N.; supervision, A.D. All authors have read and agreed to the published version of the manuscript.

References

1. Jenkins, M.G.; Salem, J.A.; Helfinstine, J.; Quinn, G.D.; Gonczy, S.T. International standards for properties and performance of advanced ceramics—30 years of excellence. In *Mechanical Properties and Performance of Engineering Ceramics and Composites XI*; Salem, J., Singh, D., Eds.; The American Ceramic Society: Columbus, OH, USA, 2019.
2. Ferraris, E.; Vleugels, J.; Guo, Y.; Bourell, D.; Kruth, J.P.; Lauwers, B. Shaping of engineering ceramics by electro, chemical and physical processes. *CIRP Ann.* **2016**, *65*, 761–784. [CrossRef]
3. Rakshit, R.; Das, A.K. A Review on Cutting of Industrial Ceramic Materials. *Precis. Eng.* **2019**, *59*, 90–109. [CrossRef]
4. Li, R.W.K.; Chow, T.W.; Matinlinna, J.P. Ceramic dental biomaterials and CAD/CAM technology: State of the art. *J. Prosthodont. Res.* **2014**, *58*, 208–216. [CrossRef] [PubMed]
5. Wongkamhaeng, K.; Dawson, D.V.; Holloway, J.A.; Denry, I. Effect of Surface Modification on In-Depth Transformations and Flexural Strength of Zirconia Ceramics. *J. Prosthodont.* **2018**, *28*, E364–E375. [CrossRef] [PubMed]
6. Davim, J.P. *Nontraditional Machining Processes*; Springer: London, UK, 2013.

7. Dolimont, A. Functionalization of Electron Beam Melting Parts in Order to Guide Finishing Operations. Ph.D. Thesis, University of Mons—Faculty of Engineering, Mons, Belgium, 2018.
8. Chen, Z.; Li, Z.; Li, J.; Liu, C.; Lao, C.; Fu, Y.; Liu, C.; Li, Y.; Wang, P.; Yi, H. 3D printing of ceramics: A review. *J. Eur. Ceram. Soc.* **2019**, *39*, 661–687. [CrossRef]
9. Rane, K.; Farid, M.A.; Hassan, W.; Strano, M. Effect of printing parameters on mechanical properties of extrusion-based additively manufactured ceramic parts. *Ceram. Int.* **2021**, *47*, 12189–12198. [CrossRef]
10. Juste, E.; Petit, F.; Lardot, V.; Cambier, F. Shaping of ceramic parts by selective laser melting of powder bed. *J. Mater. Res.* **2014**, *29*, 2086–2094. [CrossRef]
11. Abdelmoula, M.; Küçüktürk, G.; Juste, E.; Petit, F. Powder Bed Selective Laser Processing of Alumina: Scanning Strategies Investigation. *Appl. Sci.* **2022**, *12*, 764. [CrossRef]
12. Suwanpreecha, C.; Manonukul, A. A Review on Material Extrusion Additive Manufacturing of Metal and How It Compares with Metal Injection Moulding. *Metals* **2022**, *12*, 429. [CrossRef]
13. Zhao, Z. Review of non-destructive testing methods for defect detection of ceramics. *Ceram. Int.* **2021**, *47*, 4389–4397. [CrossRef]
14. Garrido, I.; Barreira, E.; Almeida, R.M.; Lagüela, S. Introduction of active thermography and automatic defect segmentation in the thermographic inspection of specimens of ceramic tiling for building façades. *Infrared Phys. Technol.* **2022**, *121*, 104012. [CrossRef]
15. Ramírez, I.S.; Márquez, F.P.G.; Papaelias, M. Review on additive manufacturing and non-destructive testing. *J. Manuf. Syst.* **2023**, *66*, 260–286. [CrossRef]
16. Malekipour, E.; Attoye, S.; El-Mounayri, H. Investigation of Layer Based Thermal Behavior in Fused Deposition Modeling Process by Infrared Thermography. *Procedia Manuf.* **2018**, *26*, 1014–1022. [CrossRef]
17. Senck, S.; Glinz, J.; Heupl, S.; Kastner, J.; Trieb, K.; Scheithauer, U.; Dahl, S.S.; Jensen, M.B. Ceramic additive manufacturing and microstructural analysis of tricalcium phosphate implants using X-ray microcomputed tomography. *Open Ceram.* **2024**, *19*, 100628. [CrossRef]
18. Servais, P.; Greffe, C.; Wallon, A.; Gandin, E. Use of micro-focus X-ray system and pulse thermography to measure porosity contentinto aerospace composite parts. In Proceedings of the 11th International Symposium on NDT in Aerospace, Paris-Saclay, France, 12–15 November 2019.
19. Bossi, R.; Georgeson, G. Nondestructive testing ofaerospace composites. In *Polymer Composites in the Aerospace Industry*; Woodhead Publishing: London, UK, 2020.
20. Nsengiyumva, W.; Zhong, S.; Lin, J.; Zhang, Q.; Zhong, J.; Huang, Y. Advances, limitations and prospects of nondestructive testing and evaluation of thick composites and sandwich structures: A state-of-the-art review. *Compos. Struct.* **2021**, *256*, 112951. [CrossRef]
21. Towsyfyan, H.; Biguri, A.; Boardman, R.; Blumensath, T. Successes and challenges in non-destructive testing of aircraft composite structures. *Chin. J. Aeronaut.* **2020**, *33*, 771–791. [CrossRef]
22. Notebaert, A.; Quinten, J.; Moonens, M.; Olmez, V.; Barros, C.; Cunha, S.S., Jr.; Demarbaix, A. Numerical Modelling of the Heat Source and the Thermal Response of an Additively Manufactured Composite during an Active Thermographic Inspection. *Materials* **2024**, *17*, 13. [CrossRef] [PubMed]
23. Ebrahimi, S.; Fleuret, J.; Klein, M.; Théroux, L.-D.; Georges, M.; Ibarra-Castanedo, C.; Maldague, X. Robust Principal Component Thermography for Defect Detection in Composites. *Sensors* **2021**, *21*, 2682. [CrossRef] [PubMed]